Materials Today Physics 65 (2026) 102128

Contents lists available at ScienceDirect

Materials Today Physics

journal homepage: www.journals.elsevier.com/materials-today-physics

Chemical ordering and non-linear magnetic behavior: enhancing magnetocaloric effect in FeMnNiGeSi high-entropy materials

V. Fournée [a,*], G. Lengaigne [a], P. Boulet [a], S. Migot [a], J. Ledieu [a], J. Tobola [b], S. Semsari Parapari [c], S. Ražnjević [c], S. Šturm [c], L. Gallo [d], S. Fabbrici [d], F. Cugini [d,e], M. Solzi [d,e], F. Albertini [d,**]

[a] Institut Jean Lamour, CNRS-Université de Lorraine, Nancy, 54011, France
[b] Faculty of Physics and App. Comp. Science, AGH University, Krakow, 30-059, Poland
[c] Jozef Stefan Institute, Department for Nanostructured Materials, Jamova cesta 39, Ljubljana, 1000, Slovenia
[d] Institute of Materials for Electronics and Magnetism (IMEM), National Research Council (CNR), Parco Area delle Scienze 37/A, Parma, 43124, Italy
[e] Department of Mathematical, Physical and Computer Sciences, University of Parma, Parco Area delle Scienze 7 A, Parma, 43124, Italy

ARTICLE INFO

Keywords:
High entropy alloys
Magnetocaloric materials
Density functional theory
Non-linear effects
Chemical order
Transition metal-based materials

ABSTRACT

High-entropy alloys (HEAs) offer opportunities to discover new functional materials with combination of properties not reached in other classes of materials. Here we report a detailed investigation of the structure, magnetic and magnetocaloric properties of some high entropy materials in the FeMnNiGeSi quinary system. Our findings indicate the persistence of partial chemical ordering, with transition metal atoms and metalloids preferentially occupying specific crystallographic sites. This ordering is further supported by *ab initio* total energy calculation. In turn, the magnetic moment - carried out mainly by Fe and Mn - exhibits a strong dependence on the crystallographic sites occupied by these magnetic atoms. By exploring the chemical landscape, we observed highly non-linear magnetic behavior upon Mn doping, resulting in an isothermal entropy change (ΔSm) as high as 35 $Jkg^{-1}K^{-1}$ in 5 T, while the transition temperature can be tuned in the range from 160 to 263 K, approaching room temperature. These outstanding performances suggest that rare-earth free high entropy materials can rival conventional magnetocaloric materials. Additionally, we find that the first-order magnetostructural transition can evolve into a second-order magnetic transition through chemical tuning. This opens the possibility of discovering similar materials near the boundary between first- and second-order transitions, with vanishing hysteresis - potentially addressing their mechanical instability issue.

1. Introduction

The development of magnetic refrigeration technologies depends on the availability of a magnetocaloric material that should fulfill several requirements [1–5]. The primary one is to exhibit as large a magnetocaloric effect (MCE) as possible, that is, the reversible change of its temperature and entropy respectively when adiabatically or isothermally magnetized/demagnetized [6]. The temperature of the transition should be adapted to the targeted applications, *i.e.* close to room temperature for magnetic refrigeration, or lower for cryogenic cooling [7,8]. Secondary requirements are also to be considered, including non-criticality of its constituent elements, high thermal conductivity, good mechanical properties and corrosion resistance as well as machinability among others. Most of the current prototypes and marketed magnetic refrigerators use expensive and critical rare earth (RE) elements, *i.e.* Gd due to its large saturation magnetization and Curie temperature (T_C) at around room temperature [2,3,9]. The MCE in this case is based on a second-order magnetic phase transition (SOMT), usually associated with a relatively small isothermal entropy change ΔSm and negligible thermomagnetic hysteresis. In contrast, first-order magnetic transition (FOMT) materials exhibit much larger ΔSm, thus enhancing the amount of transferable heat, but these materials suffer from larger hysteresis that may drastically reduce the reversible effect exploitable in thermomagnetic cycles [10–12]. In the quest of the ideal magnetocaloric material, which in principle should take the best of these two materials classes [13], high-entropy alloys (HEAs) have recently

* Corresponding author.
** Corresponding author.
E-mail addresses: vincent.fournee@univ-lorraine.fr (V. Fournée), franca.albertini@cnr.it (F. Albertini).

https://doi.org/10.1016/j.mtphys.2026.102128
Received 1 April 2026; Received in revised form 8 May 2026; Accepted 13 May 2026
Available online 21 May 2026

come in the forefront of the scene [14,15].

HEAs is a new concept for designing alloys introduced by Yeh and Cantor [16,17]. In contrast to conventional alloys - usually based on a principal element and containing secondary elements added to specifically improve a property - HEAs mix a large number of elements (five or more) at equal or near-equal concentrations. The original idea was that the resulting high configurational entropy of mixing could contribute to the stabilization of a solid solution in a simple crystallographic structure like *bcc*, *fcc* or *hcp*. HEAs have attracted considerable interests in materials science in the last two decades, mainly for their exceptional mechanical properties [18,19]. Interestingly, HEAs can exhibit non-linear effects, in the sense that some of their properties do not change proportionally or predictably with small changes in composition. This is different from conventional alloys, for which many properties follow a linear rule of mixture. An example of non-linear behavior is the dramatic increase of strength or a change in magnetism upon minor compositional change in the CoCrFeMnNi Cantor alloy [20–23].

In recent years, the focus on HEAs has shifted towards multifunctional properties, including electronic, catalytic, optical and magnetic properties [24,25]. Recent works reported promising magnetocaloric performances in several RE-based HEAs with ΔSm ~10 $Jkg^{-1}K^{-1}$ in 5 T, however with transition temperatures usually below 100 K [26–28]. The temperature of the transition can be tuned towards room temperature in transition metal based (TM) HEAs, but in these materials, the values of ΔSm were very modest ($\leq$1 $Jkg^{-1}K^{-1}$) in initial reports [29–33]. Tuning magnetocaloric HEAs towards a first-order phase transition was pivotal in enhancing their MCE up to remarkable values. This strategy was successfully applied to MM'X-type of alloys (with M,M' = TM and X = Ge, Si or Sn) but could be extended to all-d-Heusler-type or Fe_2P--type compounds in principle [34–38]. Starting from the ternary system MnNiSi presenting the targeted FOMT and applying chemical substitutions to drive the compound in the HEA domain led to the groundbreaking discovery of a set of promising quinary (FeMnNiGeSi) or senary (FeMnNiCoGeSi) magnetocaloric HEAs. In the case of FeMnNiGeSi, their MCE was evaluated from the isothermal entropy change ΔSm reaching values up to 13 $Jkg^{-1}K^{-1}$ in 2.5 T, with a magnetostructural transition temperature that can be tuned from 143 to 203 K by chemical optimization [34,35]. It was further reported that the magnetocaloric response and the transition temperature could be increased upon low-temperature heat-treatment, a fact attributed to a stress-relaxation mechanism [39]. It results from these previous reports on FeMnNiGeSi HEAs that the MCE is very sensitive to small chemical and microstructural changes in these samples.

The observed scattering of the magnetocaloric performances indicates the importance of a full structural and microstructural characterization of the materials variables that could influence their properties. A better understanding of the physical mechanisms underlying the enhanced MCE must be developed based on crystallographic, chemical and microstructural considerations.

In the following, we present a detailed investigation of the structure and magnetocaloric properties of some HEAs in the FeMnNiGeSi quinary system. Fully homogeneous samples have been obtained by heat-treatment and their crystallographic structure has been investigated by single-crystal X-ray diffraction, high-resolution scanning transmission electron microscopy and X-ray powder diffraction, complemented by *ab initio* calculations. By exploring the effect of chemical tuning, we observe strongly non-linear magnetic behavior evidenced by a 350% enhancement of the isothermal entropy change upon Mn-doping (<1 at.%). The ΔSm reaches values as high as 35 $Jkg^{-1}K^{-1}$ in 5 T (17 $Jkg^{-1}K^{-1}$ in 2 T), and the transition temperature is brought close to room temperature in heat-treated samples. Such excellent magnetocaloric performances suggest that these rare-earth free HEAs can compete with conventional magnetocaloric materials. Furthermore, we discover that the first-order magnetostructural transition can evolve into a second-order magnetic transition by changing the Si/Ge ratio. This effect could be used to reduce hysteresis effects and mechanical instability issues linked to the large volume change experienced across the structural transition. By chemically tuning the nature of the transition toward second-order magnetic phase transition, ferromagnetic ordering could be reached without an alteration in the crystal structure and thus enabling a reversible MCE in these materials.

2. Experimental and theoretical details

2.1. Sample preparation and structural characterization

HEA samples with a total mass ranging from 3 to 5 g were synthesized by arc melting or induction melting the pure elements (Fe: 99.98%, Mn: 99.99%, Ni: 99.95%, Ge, Si: 99.9999%) under a partial pressure of argon (base pressure: 10^{-6} mbar, backfilled with 700 mbar Ar). In case of arc-melting, the samples were inverted and remelted at least five times to ensure homogeneity. A mass loss typically smaller than 1% was systematically measured after each melting. Parts of the ingots were further placed in a Ta foil, sealed in an evacuated quartz tube (backfilled with 500 mbar of an Ar(95%)/H_2(5%) gas) and annealed at 1073 K for 7 days, followed by cooling to room temperature. Sample labels, nominal and measured compositions are reported in Table 1. The label *S0* refers to the nominal composition $(FeMnNi)_{66.6}(Ge_{0.45}Si_{0.55})_{33.4}$. The labels *S0-* + x% correspond to samples with nominal compositions identical to *S0* adding x% of the Mn mass contained in *S0*. The labels *S1* and *S4* explore different Ge/Si ratio compared to *S0*. All alloys have a calculated entropy of mixing ΔS_{mix} ~1.6 R, where R is the gas constant, thus fulfilling the requirement for quinary HEAs [40]. Characterization of the phases has been carried out using powder X-ray diffraction (PXRD) on a D8 Advance Bruker diffractometer using Cu Kα1 radiation ($\lambda Cu_{K\alpha1} = 1.54056$ Å). Single-crystal X-ray diffraction (SC-XRD) data were collected on a Bruker Kappa APEX-II diffractometer equipped with a mirror monochromator and a Mo Kα microfocus source ($\lambda Mo_{K\alpha} = 0.71073$ Å). The APEX2 program package (Bruker, 2004) was used for the cell refinements and data reductions. The crystal structure was solved using direct methods and refined with the SHELXL-2013 program (Sheldrick, 2008). Semi-empirical absorption correction (SADABS; Krause et al., 2015) was applied to the data. The elemental distribution was analyzed with energy-dispersive X-ray spectroscopy (EDXS) in a FEI Quanta 200 FEG scanning electron microscopy (SEM). A thin lamella was extracted by focused ion beam (FIB) milling using an FEI Helios Nanolab 600i dual beam with a gallium ion source (Thermo Fisher Scientific, Eindhoven, the Netherlands, previously FEI company). Structural analysis via selected area electron diffraction (SAED) and atomic resolution high-angle annular dark-field scanning transmission electron microscopy (HAADF-STEM) observations were carried out with a probe C_s aberration-corrected JEM-ARM200CF TEM/STEM equipped

Table 1
Sample labels, nominal (plain text) and measured (italic) compositions of the synthesized HEAs (in at.%). The compositions measured by EDXS are the ones obtained in the homogeneous samples, i.e., after annealing. The last columns provide the average valence electron number per atom for each compound, as well as the Ge/Si and TM/(Si + Ge) ratios.

Sample	Fe (%)	Mn (%)	Ni (%)	Ge (%)	Si (%)	e/a	Ge/Si	TM/(Si + Ge)
S0	22.2	22.2	22.2	15	18.4	6.88	0.81	2.0
	24.6	*22*	*24.5*	*12.8*	*16.1*		*0.79*	*2.46*
S1	24	20.4	20.5	18.5	16.6	6.80	1.11	1.85
	24.6	*21.5*	*22.9*	*18.1*	*12.9*		*1.4*	*2.22*
S4	24.2	21.3	21.5	16.3	16.7	6.90	0.98	2.03
	25.9	*21.2*	*22.9*	*15.1*	*14.9*		*1.01*	*2.33*
S0-	22.2	22.4	22.2	14.9	18.3	6.89	0.81	2.01
+1%	*22.2*	*22.6*	*21.9*	*15.2*	*18.1*		*0.84*	*2.0*
S0-	22.1	22.6	22.1	15	18.2	6.89	0.82	2.01
+2%	*22*	*22.3*	*21.7*	*15.6*	*18.4*		*0.85*	*1.94*
S0-	22.1	22.8	22.1	14.9	18.1	6.89	0.82	2.03
+3%	*22.6*	*22.9*	*22*	*15*	*17.5*		*0.86*	*2.08*

with a Centurio 100 mm^2 EDX detector (JEOL, Tokyo, Japan) operating at 200 kV (point resolution 0.12 nm in TEM mode and 0.078 nm in STEM mode). The HAADF-STEM images were denoised using a non-linear filter (NLFilter).

2.2. Magnetic characterization

The physical properties were measured using a physical property measurement system (PPMS-9) and vibrating sample magnetometer (VSM) from Quantum Design Inc. Isofield magnetization measurements with applied fields ($\mu_0 H = 0.02$, 0.5, 1, 2, 5 T) were performed on heating and cooling in the T range (50 K-300 K). In addition to characterizing the magnetic response as a function of T, the measurements enabled a detailed investigation of the hysteretic behavior associated with the martensitic transition and its dependence on the applied magnetic field. Isothermal magnetization curves for applied fields $\mu_0 H$ up to 5T were measured at different T across the transition. The measurements were performed on samples in powder form with a mass in the range of 30 to 60 mg. No specific correction due to internal demagnetization field was applied to the isothermal magnetization curves.

The Curie (T_C) and structural transition temperatures were also determined from ac magnetic susceptibility measurements performed with a homemade ac susceptometer under an alternating (500 Hz) field of 1 mT using thermomagnetic analysis (TMA), over a temperature range from 140 to 300 K. Direct adiabatic temperature change measurements were performed with a dedicated experimental setup based on a Cernox temperature sensor [41] using a cyclic protocol on cooling [42]. The sample temperature is continuously measured while the surrounding temperature is decreased at a constant rate of 2 K min^{-1} and a 1.8 T magnetic field is cyclically applied and removed.

2.3. Electronic structure calculations

In order to gain better insight into quantum mechanisms of magnetic and magnetocaloric properties of disordered FeMnNiGeSi HEA systems in hexagonal (SG *P6$_3$/mmc*, n°194) and orthorhombic (SG *Pnma*, n°62) structures, the Green function charge- and spin-self consistent Korringa-Kohn-Rostoker method with the coherent potential approximation (KKR-CPA) was used for electronic structure calculations [43–45]. The CPA model appears to be particularly well-adapted approach to investigate highly disordered materials, since it allows to account for *ab initio* computations of random atoms distribution on selective crystallographic sites. The effective medium is defined by the averaging of Green's functions ascribed to particular atoms, G_i, over their concentrations, x_i, i.e. $G_{cpa} = \Sigma_i\, x_i\, G_i$, where index i denotes either transition metal atoms (Mn, Fe, Ni) or metalloids (Si, Ge), and these CPA conditions are solved in a self-consistent way. It is really worth noting that within the CPA model, the symmetry of the unit cell is maintained in the considered range of alloy composition, for which ground state properties can be computed (density of states, magnetic moments, total energy) and then compared for different alloy compositions. The self-consistent crystal potential was constructed within the local spin-density approximation (LSDA) framework, using the Perdew-Wang formula for the exchange-correlation part. The KKR-CPA computations in disordered FeMnNiGeSi have been restricted to the muffin-tin form of crystal potential with truncations on each atom up to the angular momentum cutoff $l_{max} = 3$. For well-converged atomic charges (below 10^{-3} e) and crystal potentials (below ~10 meV), the total, site-decomposed and l-decomposed density of states (DOS) were computed using the integration tetrahedron method in reciprocal space and 560 k-space points in the irreducible part of the Brillouin zone. The total magnetic moment per Wigner-Seitz cell and all atomic magnetic moments inside muffin-tin spheres were calculated. The Fermi level, E_F, was accurately determined from the Lloyd formula [44]. In our KKR-CPA computations both core and valence states of electrons were treated in a nonrelativistic approach. It should be highlighted that all calculations were performed for the nominal systems, assuming experimentally determined lattice parameters and atomic positions.

3. Results and discussion

3.1. Structural analysis

The sample *S0* has a nominal composition corresponding to the general formula $(FeMnNi)_{66.6}(Ge_{0.45}Si_{0.55})_{33.4}$ and is derived from the ternary NiMnSi system through nearly isoelectronic chemical substitutions. The PXRD pattern recorded at room temperature indicates a pure hexagonal phase. However, a dual-phase microstructure is evident in SEM images and EDXS maps in the as-cast state (Fig. 1(a)), with regions of darker and lighter contrast within each grain corresponding to different Ge/Si ratio similar to [34]. After determining a solidus temperature of 1348 K by differential thermal analysis, a thermal-treatment at 1073 K for 7 days was applied, resulting into a chemically homogeneous single-phase sample (Fig. 1(a)). The composition measured by EDXS $Fe_{24.6}Mn_{22}Ni_{24.5}Ge_{12.8}Si_{16.1}$ is close to the nominal one. This homogenization treatment is accompanied by a narrowing of the diffraction peaks. The structure was determined from SC-XRD at room temperature and the crystallographic data are summarized in Table 2. The compound crystallizes with a hexagonal unit cell with parameters $a = 4.0283(3)$ and $c = 5.1740(6)$ Å in the $P6_{/3}mmc$ space group. The structure type is identified as FeNiGe with three Wyckoff crystallographic sites (*2a (Fe)*, *2d (Ni)*, *2c(Ge)*) and two formula units per cell (Fig. 1(b and c)).

As mentioned earlier, the realization of a full random solid solution in HEAs is only rarely achieved, except in all-RE HEAs for which the pair enthalpies of mixing and elemental atomic radii differences are negligible [46,47]. In many other HEA systems, these conditions are not strictly reached, and many of them are metastable and prone to demixing, resulting in inhomogeneities sometimes at a nanometer scale. In order to verify the sample homogeneity at a shorter length scale, a FIB lamella was extracted from the annealed *S0* and analyzed by TEM (Fig. S1). The lamella contained only few grains, most of them being oriented along the [0,1,0] zone axis (selected area electron diffraction pattern (SAED) in Fig. 2(a)). A composition profile measured by EDX along a 500 nm long line with a 27 nm step is shown in Fig. 2(b). The composition does not show any significant variation on that length scale and the line-averaged composition is similar to the one reported above, thus confirming chemical homogeneity at the nanoscale.

Another important question to be addressed is the possible chemical ordering among the crystallographic sites. Are all the three Wyckoff positions of the hexagonal unit cell randomly occupied by all atomic species, or is there any partial ordering between the transition metal (TM) atoms and the metalloids in the quinary system? HAADF-STEM is a method of choice to answer this question due to its $\overline{Z}^{1.7}$ contrast dependence of the atomic column, with $\overline{Z}$ the average atomic number of the atoms constituting the column. Along the [0,1,0] zone axis of the FeNiGe structure type, each atomic column is monoelemental. Therefore, if the (*2a*,*2d*) crystallographic sites were occupied by the TM atoms and the (*2c*) by the metalloids like in the parent ternary phase, taking into account the composition of the quinary phase, the atomic columns of the TM should be 30% more intense compared to the metalloid ones. However, the *2d* (Ni) and *2c* (Ge) columns are separated by a distance of only 1.14 Å and are therefore difficult to resolve, thus producing an elongated shape in the [210] direction as can be seen in the HAADF-STEM image shown in Fig. 2(c). Examples of line profiles taken along this direction (inset of Fig. 2(c)) either show a doublet of peaks with similar intensities or a single broader, elongated peak when the doublet is not resolved. In some other parts, the intensity distribution is more asymmetric as would be expected for selected occupancies of these two crystallographic sites. It is therefore difficult to conclude from HAADF-

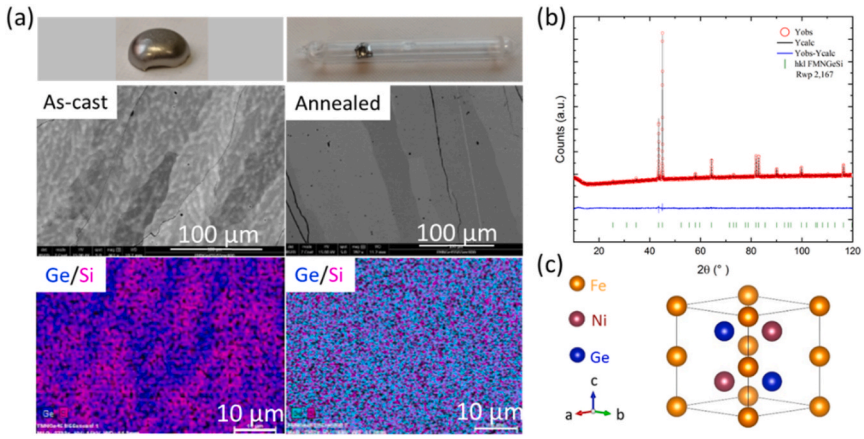

Fig. 1. (a) Optical images, backscattered electron micrographs and corresponding Ge/Si EDXS maps of $(FeMnNi)_{66.7}(Ge_{0.45}Si_{0.55})_{33.3}$ sample S0 in the as-cast state (left column) and after annealing (right column). (b) Rietveld refinement of powder x-ray diffraction pattern recorded at room temperature after annealing showing a pure hexagonal phase with $P6_3/mmc$ space group, refined lattice parameters a = 4.029 Å, c = 5.177 Å, and FeNiGe structure type illustrated in (c).

Table 2
Precession images (sample S0) recorded at 300 K (left column) and structure refinement from single crystal XRD patterns assuming either selective occupation (central column) or full random solid solution (right column). The corresponding models are illustrated, with indication of the site symmetry occupied by the metalloids in case of partial disorder solutions.

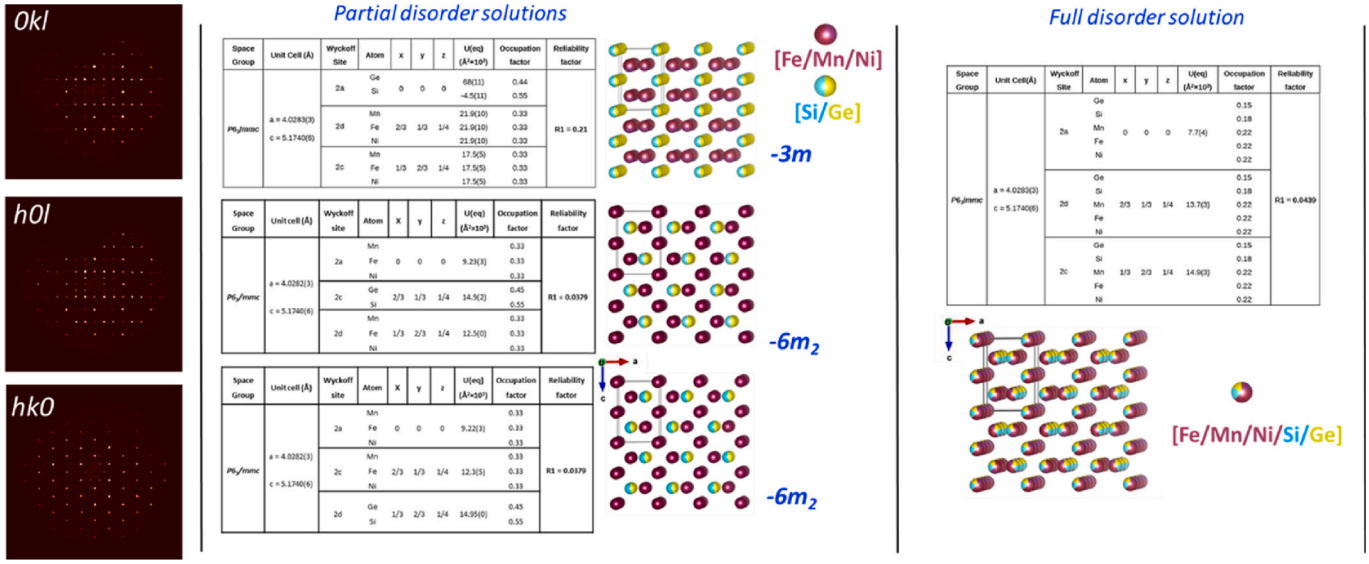

STEM analysis alone.

More information can be obtained from a structure refinement of SC-XRD patterns considering using several hypotheses. One hypothesis considers a full random distribution of all chemical species on the three Wyckoff positions while the three others consider partial ordering, in which the metalloids occupy only one type of sites and the TM atoms the two other ones (see Table 2). The reliability factor is quite high ($R_1 = 0.21$) for metalloids occupying the site *2a*, while for fully random occupation, the reliability factor is reduced to $R_1 = 0.044$. The reliability factor is slightly lower ($R_1 = 0.038$) if the metalloids occupy the site *2c*, or equivalently the site *2d* which have both the same symmetry. From these results, we conclude that all the elements are either randomly distributed on all crystallographic sites, or partially ordered with the metalloids on site *2c* or *2d*.

The HEA compound undergoes a structural transformation upon cooling towards an orthorhombic phase, the structure of which was also determined from single-crystal XRD at 90 K. The crystallographic data are summarized in Table 3. The compound crystallizes with an orthorhombic unit cell with parameters $a = 5.820(3)$, $b = 3.6674(2)$ and $c = 7.005(3)$ Å, space group *Pnma*. The structure type is identified as TiNiSi with three *4c* Wyckoff positions. The reliability factor is 0.052 for the full disorder hypothesis and slightly lower (0.044) for the partial disorder solution in which the metalloids occupy the position of Si in the parent structure. The R-factor is significantly larger ($R_1 = 0.0692$ and 0.0706) if the metalloids are placed on one of the two 4c sites of the parent structure occupied by TM atoms, consistent with the results obtained for the hexagonal phase.

The volume of the orthorhombic unit cell ($V_{orth} = 149.50$ Å^3) is roughly twice as large than that of the high temperature hexagonal phase ($V_{hex} = 72.71$ Å^3) and contains four formula units per cell instead of two. The structural relationship between the high and low temperature phases is illustrated in Fig. S2. The lattice parameters are linked by the following relationships:

$$a_{ortho} \sim a_{hexa} * \sqrt{2};\ b_{ortho} \sim c_{hexa} * \frac{1}{\sqrt{2}};\ c_{ortho} \sim a_{hexa} * \sqrt{3}$$

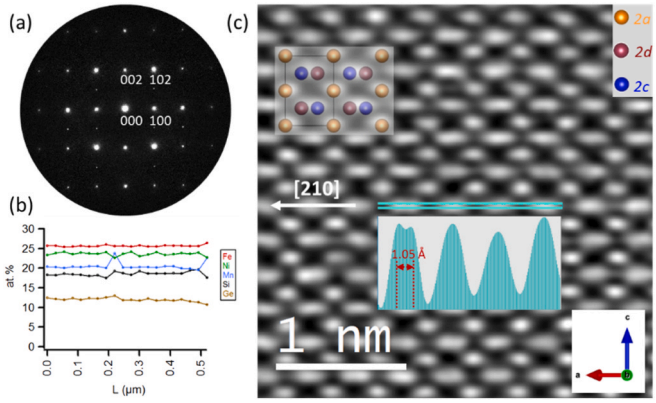

Fig. 2. (a) SAED pattern (sample S0) taken in the [0,1,0] zone axis. (b) EDX compositional profile. (c) HAADF-STEM image recorded in the same zone axis, superimposed with the FeNiGe structure type model. The inset shows the intensity profile along the dotted green line in the [210] direction.

Table 3
Precession image (S0 sample) recorded at 90 K (left column) and structure refinement from SC-XRD patterns for the full disorder hypothesis. The corresponding model is illustrated in the right column.

Space Group	Unit cell (Å)	Wyckoff site	Atom	x	y	z	U(eq) (Å²×10³)	Occupation factor	Reliability factor
Pnma	a = 5.820(3)	4c	A_1	0.65041(11)	1/4	0.94207(10)	5.1(3)	1	R1 = 0.0521
	b = 3.6674(17)	4c	A_2	0.5322(12)	1/4	0.3202(12)	6.3(3)	1	
	c = 7.005(3)	4c	A_3	0.75726(14)	1/4	0.62611(14)	7.3(3)	0.873(5)	

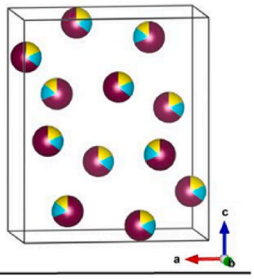

The structural transition was followed as a function of temperature between 300 K and 100 K by powder XRD, both upon cooling and heating. The acquisition time for each temperature was 2 h. The results are shown in Fig. 3, in a 2θ-range containing diffraction peaks of both the hexagonal and the orthorhombic phases. Upon cooling, the structural transition *hexa* → *ortho* starts at 145 K. This is consistent with a first order transition observed in the specific heat measurement (Fig. S3). The transition is progressive, the two phases coexisting in the range 145-120 K and at 100 K, only the orthorhombic phase can be detected. Upon annealing, the hexagonal phase reappears at ~160 K, thus with some thermal hysteresis. The orthorhombic phase cannot be detected anymore for $T \geq 170$ K. The lattice parameters and corresponding unit cell volume (V_{ortho} or $2V_{hexa}$) as a function of temperature are plotted in Fig. S4. It shows a significant increase of the material's volume across the transition *hexa* → *ortho*, on the order of 3%, the low temperature phase being the one with the largest volume (*i.e.* negative thermal expansion).

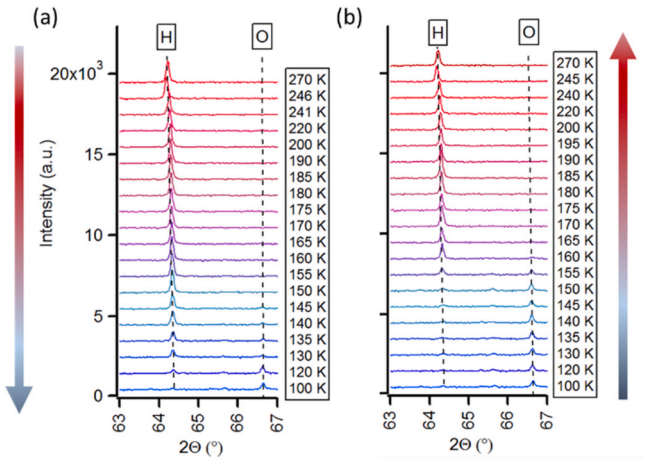

Fig. 3. Temperature dependent powder XRD patterns of $(FeMnNi)_{66.7}(Ge_{0.45}Si_{0.55})_{33.3}$ sample S0 upon cooling (a) and heating (b) showing the reversible martensitic structural phase transition hexa (H) → ortho (O). The indexation is $(202)_H$ and $(222)_O$.

3.2. Magnetic properties

In Fig. 4(a) and (b), isofield magnetic measurements on heating and cooling are shown. At low field ($\mu_0 H = 20$ mT) the magnetization on heating shows an abrupt increase at 161 K corresponding to the structural martensitic transformation from orthorhombic to hexagonal structure, followed by a decrease at the ferromagnetic to paramagnetic (FM→PM) Curie transition at 189 K, consistent with the peak observed in the $C_p(T)$ (Fig. S3). Upon cooling, the magnetization shows a sharp paramagnetic to ferromagnetic (PM→FM) transition at 189 K (Fig. 4(a)). On further cooling, the magnetization decreases abruptly to a lower value at 145 K corresponding to the structural transition. While the critical temperature for the second-order Curie transition is identical on heating and cooling, the first-order structural transition shows a thermal hysteresis of 16 K. A similar behavior, characterized by an increase of signal on heating at the structural transition, is also observed for 0.5 T (Fig. 4(b)). At such low fields, the signal is governed by the magneto-crystalline anisotropy of the two phases. In fact, the phase stable at lower T has the lowest symmetry (orthorhombic) and the highest magnetocrystalline anisotropy, resulting in lower magnetic susceptibility with respect to the hexagonal one. The thermomagnetic analysis is consistent with a first order structural phase transition (FOPT) not concomitant with the second-order magnetic one.

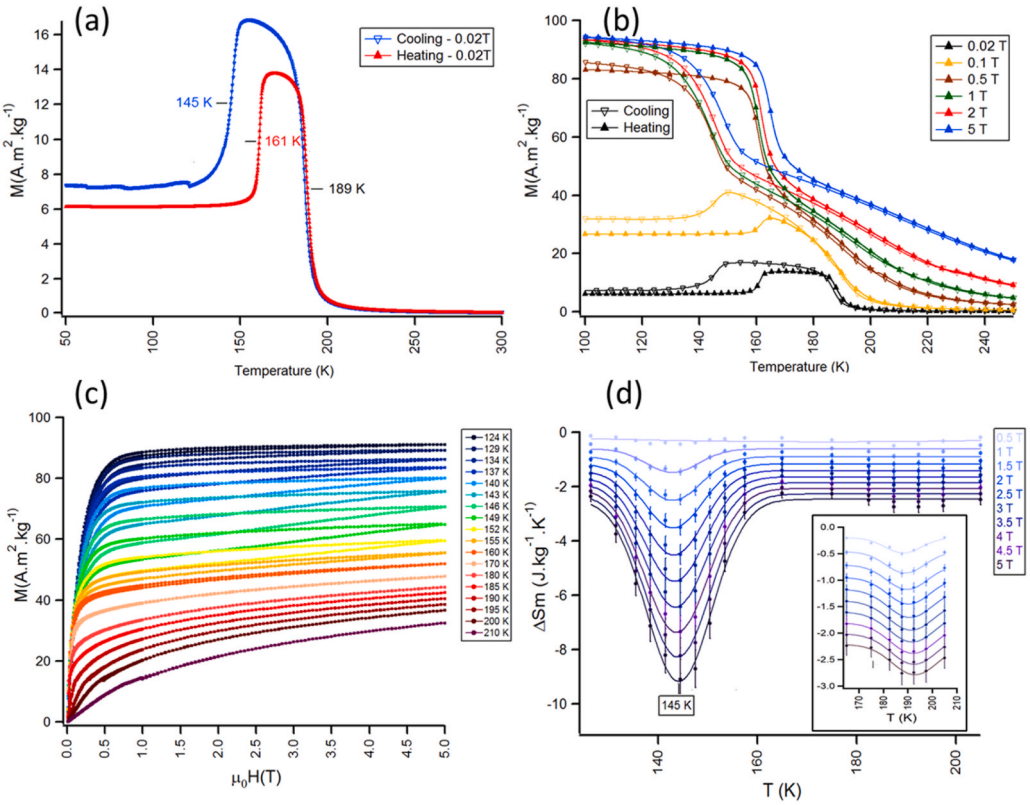

Fig. 4. Thermomagnetic measurements of $(FeMnNi)_{66.7}(Ge_{0.45}Si_{0.55})_{33.3}$ sample S0 upon cooling and heating in 0.02 T (a) and for various field up to 5 T (b). Isothermal magnetization curves M(H) (c) and calculated isothermal entropy change ΔSm (d) The inset shows the presence of a second peak at 192 K.

At higher fields (≥0.5 T), the magnetization curves display a continuous decrease upon heating, with an abrupt drop at the structural transition followed by a more gradual decrease at higher temperatures (Fig. 4(b)). In this regime the intensity is governed by the saturation magnetization value that is higher in the orthorhombic phase than in the hexagonal one.

We further measured the isothermal magnetization curves (Fig. 4(c)) for different temperatures across the transition, between 124 and 210 K. Here a discontinuous measurement protocol was used in which the sample is re-heated well above the transition ($T_{reset} = 300$ K) and then cooled to the next temperature for each M(H) measurement. This protocol ensures that the measurement loop starts with the material in the same single-phase state, unambiguously crossing the phase transition and thereby avoiding spurious hysteresis effect [42,48,49]. For temperatures below the structural transition, the magnetization increases rapidly with field, approaching saturation after 1 T with magnetization value reaching 91 Am^2kg^{-1}. The magnetization and demagnetization curves almost overlap, indicating negligible magnetic hysteresis. A hysteresis starts to develop when the temperature approaches the martensitic transition temperature where a hysteretic metamagnetic behavior is observed due to the magnetic field induced structural transformation. It becomes negligible again for T ≥ 170 K. For temperatures above T_C, the isothermal magnetization curves show a more linear aspect characteristic of a paramagnetic state.

The magnetocaloric response of the material is evaluated by calculating the isothermal magnetic entropy change Δ*Sm* using the Maxwell relation [42]:

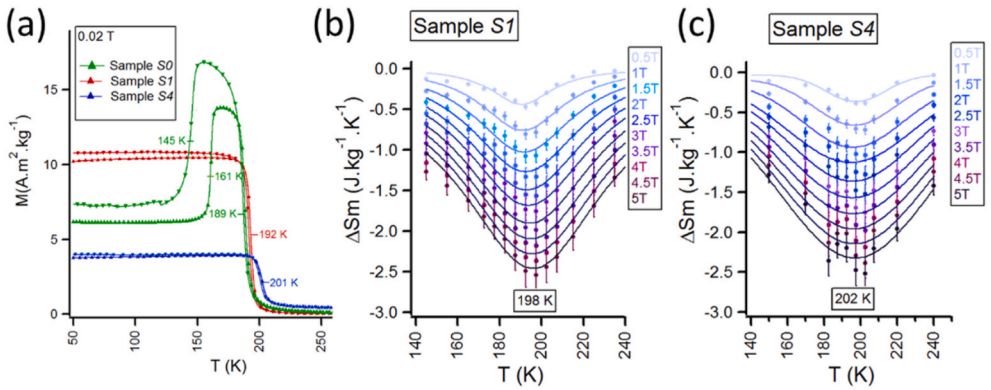

Fig. 5. Magnetization curves M(T) in 0.02 T (a) and isothermal entropy change ΔSm of samples S1 (b) and S4 (c).

$$\Delta S_m = \mu_0 \int_{Hi}^{Hf} \left(\frac{\partial M}{\partial T}\right)_H \quad (1)$$

Fig. 4(d) shows the temperature dependence of ΔSm in a magnetic field of 0-5 T. A peak maximum is obtained at 145 K, reaching a $|\Delta Sm|$ value of 9.2 $JKg^{-1}K^{-1}$ in 5 T (3.5 $JKg^{-1}K^{-1}$ in 2 T), and a full width at half maximum of ~20 K. The peak value is similar to the one reported in Ref. [34] for a sample with similar composition in the as-cast state. In addition, the peak maximum in $|\Delta Sm|$ occurs at the martensitic transition temperature rather than at the Curie (T_C) temperature. A second maximum is observed at 192 K ~ T_C (inset of Fig. 4(d)), with peak value of 2.7 $JKg^{-1}K^{-1}$ in 5 T. It suggests that the lattice contribution is the dominant contribution to the entropy change.

3.3. Effect of chemical tuning

With the aim to align the structural and magnetic transitions to enhance the magnetocaloric effect [50], additional samples were synthesized with slightly different compositions compared to *S0* (see Table 1).

3.3.1. Effect of Ge/Si ratio

The magnetization curves for sample *S1* and *S4* (Fig. 5(a)), which are isostructural to *S0* but with higher Ge/Si ratio compared to sample *S0* (Table 1), only show a PM→FM transition at T_C~192 K and 201 K in 20 mT respectively, with no evidence for a structural FOPT. Indeed, *S1* and *S4* remain hexagonal between 300 K and 90 K (see XRD patterns in Fig. S5). The corresponding magnetocaloric response evaluated through the isothermal magnetic entropy change ΔSm (Fig. 5(b and c)) shows a very broad peak at ~ T_C with a full width at half maximum of ~90 K and with peak value of about 2.5 $JKg^{-1}K^{-1}$ in 5 T, therefore much lower than the values obtained for *S0*. A direct reversible adiabatic temperature change of 0.5 K in 1.8 T at ~200 K was also measured for both samples. Here only the spin system contributes to the entropy change, contrary to sample *S0*. Such strong variations of the magnetocaloric effect in sample *S1* and *S4* compared to sample *S0*, correlated with minute compositional changes, evidence a non-linear magnetic behavior in this system.

3.3.2. Effect of Mn-doping

A series of samples *S0- + x%* (x = 1,2 and 3, see Table 1) was prepared by adding x% of the Mn mass contained in sample *S0*. This results in small nominal composition changes, less than 1 at.%. The measured compositions given in Table 1 confirm a small enrichment in Mn, but also in metalloids Si and Ge, and a corresponding reduction in Fe and Ni. The Ge/Si ratio is similar to that in *S0*, but the TM/metalloid ratio are smaller in the *S0- + x%* series compared to that measured in *S0* (see Table 1). Isostructural samples are obtained across the series, both in the as-cast and annealed states (Fig. S6). All samples *S0- + x%* undergo a FOPT from *hexa (H)* at room temperature to *ortho (O)* upon cooling as evidenced by powder XRD (Fig. S6). They contain a very small fraction of an impurity phase with a measured composition $Fe_{8.7}Mn_{32.5}Ni_{32.7}Ge_{5.5}Si_{20.5}$ that can be detected in EDX map (not shown here) but hardly in the XRD patterns. The thermomagnetic analysis shows a single jump in the *ac* susceptibility (Fig. 6(a)) suggesting that the structural transition is now concomitant with the PM→FM transition. Interestingly, the T_C increases upon Mn-doping, and increases further upon annealing (Fig. 6(a)). In the as-cast state, the Mn-doped samples have a T_C ranging from 218 to 234 K while in the annealed state, T_C ranges from 255 to 263 K, *i.e.* close to room temperature.

The magnetization curves as a function of temperature for *S0-1%* are shown in Fig. 7(a) in low field and up to 2 T (Fig. 7(b–e)), both upon cooling and heating. A single jump in the magnetization is observed consistent with a FOPT. The transition temperature shifts by 2.7 K with increasing field up to 2 T ($dT_t/dH \approx 1.35$ K/T). A thermal hysteresis ΔT_{hyst} is observed between cooling and heating. The saturation magnetization derived from isothermal magnetization curves M(H) (Fig. 7(c–f)) approaches 100 Am^2kg^{-1} at low temperatures. The magnetocaloric response evaluated from the isothermal entropy change ΔSm shows a peak maximum reaching values of 30 $JKg^{-1}K^{-1}$ in 5 T (15 $JKg^{-1}K^{-1}$ in 2 T) both in the as-cast and annealed states (Fig. 7(d–g)). That is more than 3 times larger compared to the undoped sample. The full width at half maximum of $\Delta Sm(T)$ is less than 10 K, with peak position at 216 and 249 K for as-cast and annealed respectively.

Similar results have been obtained across the series of Mn-doped samples *$(FeMnNi)_{66.7}(Ge_{0.45}Si_{0.55})_{33.3}$ S0- + x% (x=1,2 and 3)*. The data are provided in Figs. S7 and S8 and summarized in the graph in Fig. 6(b) showing the T_C upon heating and ΔT_{hyst} measured in 2 T, as well as peak values of ΔSm in 5T for the same samples. Therefore, the joint effect of Mn-doping and annealing leads to an increase of T_C by approximately 100 K, reaching values close to room temperature, and ΔSm values up to 35 $Jkg^{-1}K^{-1}$ in 5 T, *i.e.* 3.5 times larger compared to the undoped *S0* sample. The maximum adiabatic temperature change ΔT_{ad} for a complete phase transformation can be estimated from $\Delta T_{admax} = \mu_0 \frac{T}{C_p} \frac{dH}{dT_t} \Delta M$, reaching 26 K in 5 T in our case. Here again, the strong variation of the magnetocaloric effect in samples *S0- + x%* compared to *S0* evidences a non-linear magnetic behavior in this HEA system.

3.4. Results of ab initio KKR-CPA calculations

Based on our structural analysis, we calculated the electronic structure and magnetic properties of the high-entropy alloy FeMnNiGeSi in the hexagonal and orthorhombic phases. For the hexagonal system with nominal composition $(FeMnNi)_{66.7}(Ge_{0.45}Si_{0.55})_{33.3}$, three models with different complexity of chemical disorder were considered in line with

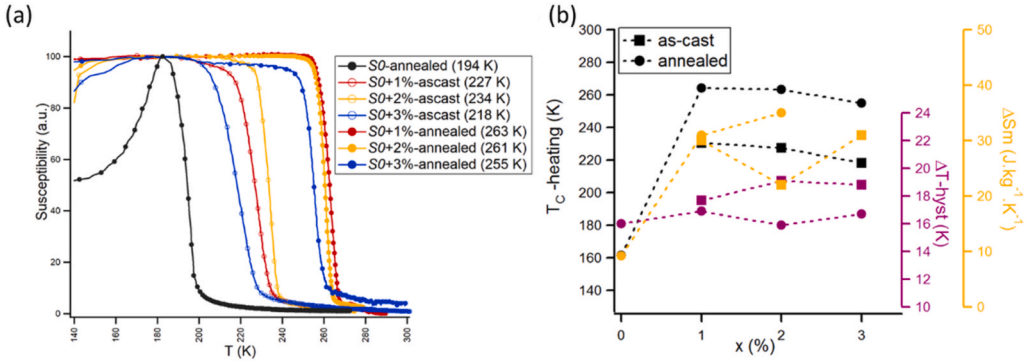

Fig. 6. (a) ac susceptibility in low applied field of 1 mT as a function of temperature, measured upon heating for samples S0 and S0-x% (x = 1, 2 and 3) for as-cast and after annealing. The corresponding T_C are mentioned in the caption. (b) Graph showing the T_C upon heating and ΔT_{hyst} measured in 2 T, as well as peak values of ΔSm in 5T for the same samples.

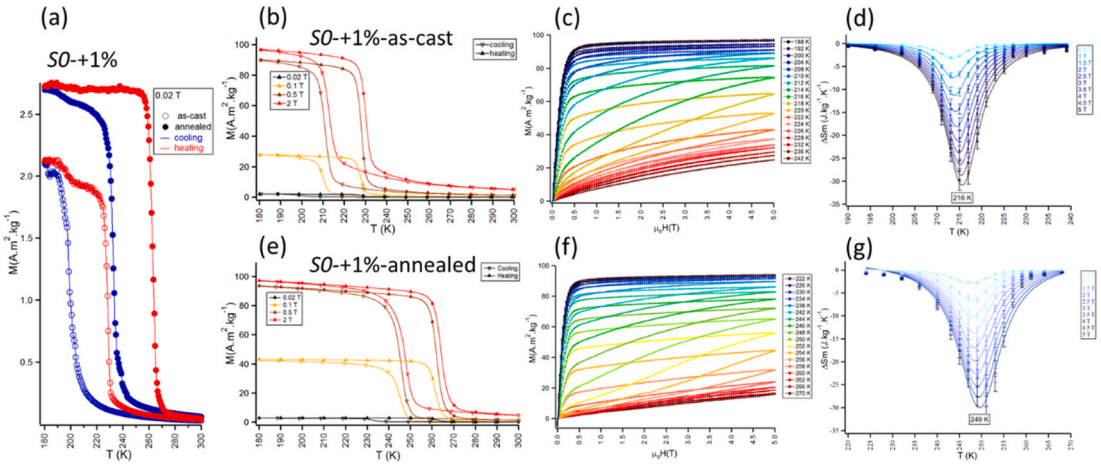

Fig. 7. Thermomagnetic measurements of the Mn-doped sample (S0-1% for as-cast and after annealing) upon cooling and heating in 0.02T (a) and in various field up to 2 T (b,e). Corresponding isothermal magnetization curves M(H) (c,f) and calculated isothermal entropy change ΔSm (d,g).

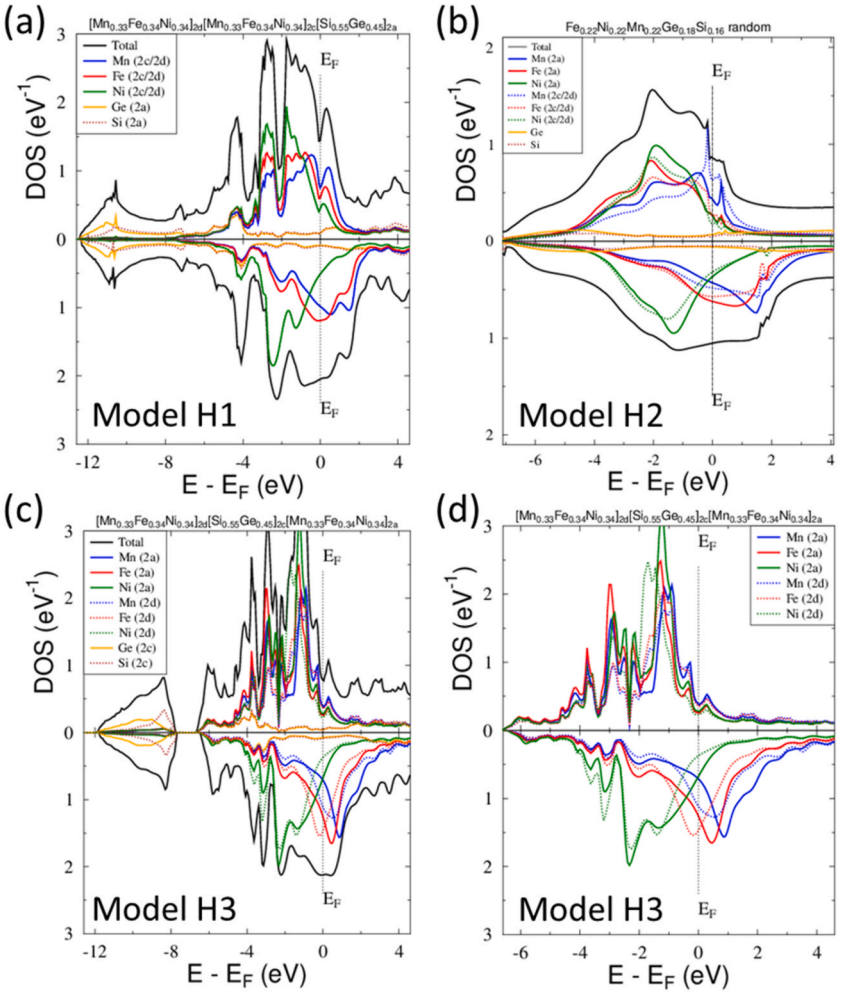

Fig. 8. KKR-CPA spin-polarized electronic DOS in hexagonal (SG $P6_3/mmc$) FeNiMnGeSi HEAs assuming three models of disordered alloys: (a) model H1 - partially disordered phase, where Fe, Ni and Mn are randomly distributed on 2c and 2d sites, while Si and Ge randomly occupy 2a site; (b) model H2 - fully disordered phase, where all five elements randomly occupy all three crystallographic sites with the same concentrations; (c,d) model H3 - partially disordered phase, where Fe, Ni and Mn are randomly distributed on 2a and 2d sites, while Si and Ge randomly occupy 2c site.

the XRD analysis. Model H1 assumed that transition metal atoms (Fe, Ni, Mn) randomly occupy the *2c* (1/3, 2/3, 1/4) and *2d* (2/3, 1/3, 1/4) positions with equivalent concentrations, while metalloid atoms (Si, Ge) preferentially occupy the *2a* (0, 0, 0) positions with concentrations of 0.55 and 0.45, respectively. Model H2 (fully disordered) assumed that all five atoms occupy the three aforementioned crystallographic

Table 4
Calculated total (per f.u.) and atomic magnetic moments (in μ_B) in three models of the hexagonal $(FeMnNi)_{66.7}(Ge_{0.45}Si_{0.55})_{33.3}$ HEA as well as in the fully disordered model H2 for the orthorhombic phase.

Model H1 ($E_{tot} = -14806.9457$ Ry)						Model H2 ($E_{tot} = -14806.8717$ Ry)					
Total	3.28					Total	5.27				
Site	Fe	Ni	Mn	Ge	Si	Site	Fe	Ni	Mn	Ge	Si
2a	-	-	-	−0.33	−0.04	*2a*	2.17	0.32	2.46	−0.04	−0.06
2c	1.22	0.07	1.21	-	-	*2c*	1.80	0.31	1.52	−0.04	−0.05
2d	1.22	0.07	1.20	-	-	*2d*	1.80	0.31	1.52	−0.04	−0.05
Model H3 ($E_{tot} = -14807.0577$ Ry)						Model H2 Orthorhombic					
Total	Total					Total	7.87				
Site	Fe	Ni	Mn	Ge	Si	Site	Fe	Ni	Mn	Ge	Si
2a	2.05	0.15	2.47	-	-	*A1*	1.50	0.22	0.27	−0.02	−0.03
2c	-	-	-	-0.05	-0.0	*A2*	2.54	0.27	3.04	−0.01	−0.03
2d	1.23	0.03	1.94	-	-	*A3*	1.35	0.22	0.06	−0.02	−0.04

positions randomly, however with concentrations adjusted accordingly, so that the alloy composition in the two hexagonal models is identical (see Table 2 for details). Model H3 was very close to model H1 concerning the complexity level of chemical disorder, but with the exchange of occupation of positions *2a* and *2c*, namely the transition metal atoms (Fe, Ni, Mn) randomly occupy the *2a* (0, 0, 0) and *2d* (2/3, 1/3, 1/4) positions with equivalent concentrations, while metalloid atoms (Si, Ge) are preferentially located at the *2c* (1/3, 2/3, 1/4) positions with concentrations of 0.55 and 0.45, respectively.

Fig. 8(a) presents total and site-decomposed DOS in model H1 for ferromagnetic state. Spin-polarization of electronic states yields total magnetic moment of 3.28μ_B (per f.u.), resulting essentially from local magnetic moments on TM atoms with the values of 1.22μ_B (Fe), 1.21 μ_B (Mn), whereas the values on Ni and metalloid atoms are negligible. It is worth noting that even in the chemically disordered model H1, the nearest atomic environment for the *2c* and *2d* positions is quite similar, which results in the self-consistent spin-polarized DOS for Fe, Mn, and Ni (mainly of *d*-states) being also very similar. In consequence, the magnetic moments of transition metal atoms at these two positions are very similar (see Table 4).

The magnetic properties of the fully disordered phase (model H2) and partially disordered phase (model H3 with inverted occupancies of sites *2a* and *2c* with respect to model H1) are markedly different from the aforementioned results for model H1. The reason for much larger magnetization (5.27 μ_B and 5.16 μ_B in models H2 and H3, respectively), can be investigated from the values of local magnetic moments (Table 4) as well as from the corresponding spin-polarized DOS shown in Fig. 8 (b–c).

It is worth noting that the presence of transition metals on site *2a* generally enhances the magnetic moments on all crystallographic sites with respect to the values computed in model H1 (see Table 4). However, what is most striking is the markedly stronger polarization of the *d*-states on the Fe and Mn atoms (but also on Ni) at the *2a* position (best seen in Fig. 4(d)). This results in much larger magnetic moments of Fe (2.17 μ_B and 2.05 μ_B for models H2 and H3) and Mn (2.46 μ_B and 2.47 μ_B for models H2 and H3) at this crystallographic site with respect to those calculated on *2c* and *2d* positions.

The measured magnetization value for sample *S0* is 90 Am^2kg^{-1} ~5.22 μB per f.u., which is very similar to the calculated ones for model H2 and H3.

In the fully disordered model H2 for the orthorhombic phase, the magnetic moment (7.87 μ_B per f.u.) mainly results from Fe and Mn atoms (but also Ni). The moments strongly depend on the crystallographic sites, especially those carried out by the Mn atoms. The calculated magnetization is ~67.8 Am^2kg^{-1}, lower than that of the corresponding hexagonal phase, which is consistent with the drop in magnetization observed during the $H \rightarrow O$ transition (Fig. 4(a)). The Curie temperature was calculated for model H2 and is ~230 K, in quite good agreement with the experimental one.

Interestingly, the KKR-CPA calculations of the total energy clearly indicates model H3 as the most favorable, in line with the XRD refinements. This supports the idea that some chemical order between TM atoms and metalloids is preserved in the HEA system. In the strict definition of a HEA, all atomic species should be randomly distributed on all crystallographic sites. Both theoretical and experimental results indicate that this criterion is not met in the FeMnNiGeSi alloys, even though the situation in the real material is probably intermediate between H1 and H3. Therefore, it is more appropriate to call them high entropy materials (HEMs) rather than high entropy alloys (HEAs), because of the remaining chemical ordering is incompatible with a solid solution phase.

While partial chemical ordering is demonstrated, we now discuss in more details its thermodynamic origin and its impact on exchange interactions and magnetic instability. The reason why it is energetically preferred to have TM in *2a* and *2d*, compared to *2c* and *2d*, must be related to the coordination polyhedral around the different crystallographic positions. Indeed, the local environment around *2a* sites (bicapped hexagonal prism with coordination number CN 14) differs from that of *2c* and *2d* sites (pentacapped trigonal prism with CN 11). This results in substantially different interatomic distances, namely ~2.66 Å between *2a* and *2d* as well as *2a* and *2c* sites, against only ~2.32 Å between *2d* and *2c* sites. The partial order has an impact on the magnetic properties. Indeed, the calculations highlight much larger magnetic moments carried by Fe and Mn at *2a* positions compared to those calculated on *2c* and *2d* positions. In Fig. S10 of the Supplementary Material, the non-spin-polarized DOS calculated for models H1 and H3 are shown. In the case of the most favorable model H3, and in view of the Stoner criterion, it is clearly observed that the magnetic interactions are enhanced on *2a* sites, which is particularly obvious for Fe and Mn, where the Fermi level falls into large *d*-DOS peak, yielding large magnetic moments, as obtained from the spin-polarized KKR-CPA computations (see Table 4). Conversely, smaller *d*-DOS of Fe and Mn on *2c*/*2d* sites resulted in much smaller values of magnetic moments. In the case of the less favorable model H1, the non-spin-polarized DOS shows a much smaller *d*-DOS peaks for Fe and Mn at the Fermi level, and in consequence of the Stoner mechanism, produces much lower magnetic moments, as obtained from spin-polarized KKR-CPA computations.

This behavior comes from stronger overlapping of wave functions of surrounding atoms due to much shorter *2c*-*2d* sites distance than the *2a*-*2c* (and also *2a*-*2d*) ones. The results obtained for these two partially ordered models (H1 and H3) can be compared with the random case (model H2), which is the least energetically favorable, although its calculated total magnetic moment is similar to model H3. From Fig. 8(b) one can notice that additional disorder between transition metal atoms and metalloids on the same crystallographic sites tend to broaden *d*-DOS peaks of Fe and Mn and decreasing their values at E_F, being unfavorable

for magnetic interactions.

Another interesting observation results from the calculations of the number of electrons inside the muffin-tin spheres (the calculations assumed identical radii for the three non-equivalent positions) for two hexagonal phase models (H2 and H3). This allows for a comparison of the self-consistent crystal potentials for different cases of chemical disorder as well as chemical bonding between atoms. We can conclude that the introduction of additional disorder in the form of Ge and Si atoms at each non-equivalent position reduces the attractive force of the crystal potential for all transition metal atoms, which to some extent can be translated into a decrease in its crystalline stability. It can be seen from Table T1 that the model H2 (fully random) has a systematically lower number of electrons around Fe, Ni, and Mn by approximately 0.15 (Mn), 0.20 (Fe), and 0.10 (Ni) electrons, with respect to the corresponding values computed for the H3 (partially disordered) model.

Finally, to get some insight into the quantitative impact of the partial order on the exchange interactions, the various contributions to the computed energies were analyzed. The potential energy E(pot), Madelung E(Mad), kinetic E(kin), band E(band) and exchange-correlation E (excor) energies are listed in Table T2 (Supplementary Material) for each model. The results converge to the conclusion that exchange-correlation energy is responsible for the lowering of the total energy in model H3. The most energetically favorable case (model H3) in view of both E(tot) and E(excor) contributions is also the one with the highest positive band energy E(band), which likely comes from the highly structured DOS character in model H3 (see Fig. 8).

4. Conclusions

In summary, the detailed structural characterization of the HEAs formed in the FeMnNiGeSi system in their annealed state demonstrate the formation of single-phase samples, that are chemically homogeneous down to the nanoscale. At the atomic scale, we have discussed different hypotheses regarding the site occupation – either fully random or partially random. Taking into account results from both experiments and *ab initio* total energy calculations, we conclude that some chemical order between the TM atoms and the metalloids is preserved while transforming the ternary MM'X system into a quinary alloy by chemical substitution. The magnetic moment - carried out mainly by Fe and Mn atoms - strongly depends on the crystallographic sites occupied by these atoms. This partial chemical order could be expected considering the different chemical bonding nature between TM atoms and metalloids. The above conclusions should be taken into consideration in the design of new HEA, as it implies that the TM/metalloid concentration ratio should be kept close to 2, similar to the ternary parent phase, in order to respect the chemical order. Additionally, the chemical order strongly influences the magnetic properties of the compound as we have seen from the *ab initio* calculations.

The chemical homogeneity in annealed samples is correlated with a significant increase of the critical temperature when compared to as-cast samples. The change in the T_C may be influenced by the sample homogeneity itself and/or by a possible stress-released mechanism associated with a slower cooling-rate in the annealed samples compared to the as-cast ones [39]. It is also found that Mn-doping is efficient in tuning T_C towards room temperature. The Mn-doped samples furthermore exhibit a structural transition that is concomitant with the magnetic one, resulting in a strong enhancement of the isothermal entropy change. The maximum value obtained $\Delta Sm \sim 35$ Jkg^{-1}K^{-1} in 5 T is very high and competitive with respect to other related high entropy magnetocaloric materials reported so far (see Table T1 in the Supplementary Material), but still lower than the maximum entropy variation (~45 Jkg^{-1}K^{-1}) which can be estimated from the Clausius-Clapeyron equation for a complete first-order transition $\Delta S_{Tmax} = -\mu_0 \frac{dH}{dT_t} \Delta M$, with ΔM the magnetization difference between the two phases and (dTt/dH) the sensitivity of the transition temperature to the magnetic field (~2 to 4 K in 2T). The maximum adiabatic temperature change ΔT_{ad} for a complete phase transformation can be estimated from $\Delta T_{admax} = \mu_0 \frac{T}{C_p} \frac{dH}{dT_t} \Delta M$, reaching 26 K in 5 T in our case. These values are very attractive for magnetocaloric applications and should be confirmed in the future by direct adiabatic temperature change measurements. Such measurements were not possible so far for first-order FeMnNiGeSi samples due to the mechanical instability induced by the large volume change across the structural transition. Cycling the material across the transition leads to the progressive transformation of the material into powders, preventing to keep a good thermal contact necessary for such measurements, while the characteristics of the magnetic transition are not altered. The stability of the thermomagnetic transition upon cycling was verified by monitoring the transition temperature by means of thermomagnetic analysis. This is illustrated in Fig. S9 showing the ac susceptibility measured in low applied field upon heating for sample *S0-1%* in the annealed state. The experiment was conducted up to 30 times, showing a stable transition with $T_{tr} = 263.6$ K. The mechanical instability is an issue that could be overcome in future works, either by controlling the microstructure of the samples using a directional solidification method for example as reported in [51] or by embedding the magnetocaloric material into a suitable composite material.

Finally, our results evidenced non-linear magnetic behaviors in these high entropy materials, driven by the competing magnetic interactions between multiple principal elements. On the one hand, minute addition of Mn resulted in a beneficial 350% in the isothermal entropy change. On the other hand, we discovered that the first-order magnetostructural transition can evolve into a second-order magnetic transition by fine-tuning the Si/Ge or metalloid/TM ratios. The latter opens the possibility to find HEAs being at the boundary between first- and second-order transition with vanishing hysteresis, which could also solve the mechanical instability issue in future work. The magnetostructural transition is usually rooted in the interplay between electronic, magnetic, and lattice degrees of freedom [52]. In the case of first-order transition from a ferromagnetic FM to a paramagnetic PM phase, the system possess two distinct energy minima separated by a finite energy barrier, leading to a discontinuous first-order transition. The energy landscape is shaped by both electronic, magnetic and lattice degrees of freedom. Chemical modifications can tune the depth and position of these minima, affecting the transition temperature and also hysteresis. In some cases, chemical modifications can flatten the free energy landscape, reducing the depth of the minima and the barrier height, leading to a continuous second-order transition. This has been observed in different magnetocaloric materials [53–58]. A similar chemically induced crossover from first-to second-order could be at play also in our high entropy material.

Finally, the finding that a chemical order is maintained while driving MM'X-type of alloys in the HEA domain is of general applicability and should be taken into consideration when extending the proposed design strategy to other families of magnetocaloric materials such as all-d-Heusler-type or Fe_2P-type compounds. In addition, the strongly non-linear magnetic behavior identified in this work is also expected to be broadly applicable to other high entropy materials, opening new possibilities for designing next generation magnetocaloric compounds and advanced materials.

CRediT authorship contribution statement

V. Fournée: Conceptualization, Data curation, Formal analysis, Funding acquisition, Investigation, Methodology, Supervision, Validation, Writing – original draft, Writing – review & editing. **G. Lengaigne:** Investigation, Validation. **P. Boulet:** Investigation, Validation. **S. Migot:** Investigation, Validation. **J. Ledieu:** Investigation, Validation, Writing – review & editing. **J. Tobola:** Formal analysis, Investigation, Validation, Writing – original draft, Writing – review & editing. **S. Semsari Parapari:** Investigation, Validation, Writing – review & editing. **S. Ražnjević:** Formal analysis, Writing – review & editing. **S. Šturm:**

Formal analysis, Funding acquisition, Writing – review & editing. **L. Gallo:** Formal analysis, Investigation, Writing – review & editing. **S. Fabbrici:** Formal analysis, Investigation, Writing – review & editing. **F. Cugini:** Formal analysis, Investigation, Writing – review & editing. **M. Solzi:** Formal analysis, Investigation, Writing – review & editing. **F. Albertini:** Conceptualization, Formal analysis, Funding acquisition, Investigation, Methodology, Supervision, Validation, Writing – original draft, Writing – review & editing.

Declaration of competing interest

The authors declare the following financial interests/personal relationships which may be considered as potential competing interests: Franca Albertini reports financial support was provided by European Union. Saso Sturm reports financial support was provided by Slovenian Research and Innovation Agency. If there are other authors, they declare that they have no known competing financial interests or personal relationships that could have appeared to influence the work reported in this paper.

Acknowledgments

This work was supported by « Lorraine Université d'Excellence », part of the France 2030 Program, reference ANR-15-IDEX-04-LUE, and the European Integrated Center for the Development of New Metallic Alloys and Compounds (ECMetAC). The authors acknowledge financial support for this research from the Slovenian Research and Innovation Agency (ARIS) under grant number P2–0084. The Project was partially funded by the European Union – NextGenerationEU under the National Recovery and Resilience Plan (NRRP), Mission 4 Component 2 Investment 1.1 - Call for tender N°.1409 of 14–09–2022 of Italian MUR (Project Code P2022KMXBL, Concession Decree No. 0001381 of 01/09/2023 adopted by the Italian MUR, CUP D53D23019360001). VF acknowledges support of the CNR through its short-term mobility program.

Appendix A. Supplementary data

Supplementary data to this article can be found online at https://doi.org/10.1016/j.mtphys.2026.102128.

Data availability

Data will be made available on request.

References

[1] E. Brück, Developments in magnetocaloric refrigeration, J. Phys. D Appl. Phys. 38 (2005): R381, https://doi.org/10.1088/0022-3727/38/23/R01.
[2] O. Gutfleisch, M.A. Willard, E. Brück, C.H. Chen, S.G. Sankar, J.P. Liu, Magnetic materials and devices for the 21st century: stronger, lighter, and more energy efficient, Adv. Mater. 23 (2011) 821–842, https://doi.org/10.1002/adma.201002180.
[3] A. Kitanovski, J. Tusek, U. Tomc, U. Plaznik, M. Ozbolt, A. Poredos, Magnetocaloric Energy Conversion: from Theory to Applications, Springer, Green Energy and Technology, 2015.
[4] V. Franco, J.S. Blàzquez, J.J. Ipus, J.Y. Law, L.M. Moreno-Ramírez, A. Conde, Magnetocaloric effect: from materials research to refrigeration devices, Prog. Mater. Sci. 93 (2018) 112–232, https://doi.org/10.1016/j.pmatsci.2017.10.005.
[5] T. Gottschall, K.P. Skokov, M. Fries, A. Taubel, I. Radulov, F. Scheibel, D. Benke, S. Riegg, O. Gutfleisch, Making a cool choice: the materials library of magnetic refrigeration, Adv. Energy Mater. 9 (2019): 1901322, https://doi.org/10.1002/aenm.201901322.
[6] Weiss and Picard, 1917.
[7] Y. Zhang, Y. Na, X. Liu, J. Xiang, F. Chen, H.-F. Li, P. Sun, S. Zhou, X. Zhang, L. Li, Refrigeration down to 0.16 K using a frustrated magnet $Gd_2B_2MoO_9$, Nat. Commun. 17 (2026) 1554, https://doi.org/10.1038/s41467-025-68278-z.
[8] L. Attou, K. El Maalam, S.-E. Bouzarmine, S. Ait Jmal, Z. El Kacemi, M. Ben Ali, S. Naamane, O. Mounkachi, P. Fournier, M. Balli, Phase-dependent structural and magnetic properties of $NdPO_4$ nanorods for cryo-magnetocaloric cooling, Mater. Today Phys. 60 (2026): 101989, https://doi.org/10.1016/j.mtphys.2025.101989.
[9] G.V. Brown, Magnetic heat pumping near room temperature, J. Appl. Phys. 47 (8) (1976) 3673–3680, https://doi.org/10.1063/1.323176.
[10] V.K. Pecharsky, K.A. Gschneidner Jr., Giant magnetocaloric effect in $Gd_5(Si_2Ge_2)$, Phys. Rev. Lett. 78 (1997) 4494, https://doi.org/10.1103/PhysRevLett.78.4494.
[11] V. Franco, J.S. Blàzquez, B. Ingale, A. Conde, The magnetocaloric effect and magnetic refrigeration near room temperature: materials and models, Annu. Rev. Mater. Res. 42 (2012) 305–342, https://doi.org/10.1146/annurev-matsci-062910-100356.
[12] J. Liu, T. Gottschall, K.P. Skokov, J.D. Moore, O. Gutfleisch, Giant magnetocaloric effect driven by structural transitions, Nat. Mater. 11 (2012) 620–626, https://doi.org/10.1038/nmat3334.
[13] O. Gutfleisch, Mastering hysteresis in magnetocaloric materials, Phil. Trans. R. Soc. A 374 (2016): 20150308, https://doi.org/10.1098/rsta.2015.0308.
[14] J.Y. Law, V. Franco, Review on magnetocaloric high-entropy alloys: design and analysis methods, J. Mater. Res. 38 (2023) 37–51, https://doi.org/10.1557/s43578-022-00712-0.
[15] J.Y. Law, L.M. Moreno-Ramirez, Á. Díaz-García, V. Franco, Current perspective in magnetocaloric materials research, J. Appl. Phys. 133 (2023): 040903, https://doi.org/10.1063/5.0130035.
[16] J. Yeh, S. Chen, S. Lin, J. Gan, T. Chin, T. Shun, C. Tsau, S. Chang, Nanostructured high-entropy alloys with multiple principal elements: novel alloy design concepts and outcomes, Adv. Eng. Mater. 6 (2004) 299–303, https://doi.org/10.1002/ADEM.200300567.
[17] B. Cantor, I. Chang, P. Knight, A. Vincent, Microstructural development in equiatomic multicomponent alloys, Mater. Sci. Eng., A 375−377 (2004) 213–218, https://doi.org/10.1016/j.msea.2003.10.257.
[18] D.B. Miracle, O.N. Senkov, A critical review of high entropy alloys and related concepts, Acta Mater. 122 (2017) 448–511, https://doi.org/10.1016/j.actamat.2016.08.081.
[19] E.P. George, D. Raabe, R.O. Ritchie, High-entropy alloys, Nat. Rev. Mater. 4 (2019) 515–534, https://doi.org/10.1038/s41578-019-0121-4.
[20] B. Gludovatz, A. Hohenwarter, D. Catoor, E.H. Chang, E.P. George, R.O. Ritchie, A fracture-resistant high-entropy alloy for cryogenic applications, Science 345 (6201) (2014) 1153–1158, https://doi.org/10.1126/science.1254581.
[21] E.J. Pickering, N.G. Jones, High-entropy alloys: a critical assessment of their founding principles and future prospects, Int. Mater. Rev. 61 (3) (2016) 183–202, https://doi.org/10.1080/09506608.2016.1180020.
[22] S. Drescher, S. Seils, T. Boll, A. Kauffmann, M. Heilmaier, J. Freudenberger, Solid solution strengthening in single-phase Au-Cu-Ni-Pd-Pt-based high-entropy alloys, J. Alloys Compd. 1002 (2024): 175273, https://doi.org/10.1016/j.jallcom.2024.175273.
[23] A. Smekhova, A. Kuzmin, K. Siemensmeyer, C. Luo, J. Taylor, S. Thakur, F. Radu, E. Weschke, A.G. Buzanich, B. Xiao, A. Savan, K.V. Yusenko, A. Ludwig, Local structure and magnetic properties of a nanocrystalline Mn-rich Cantor alloy thin film down to the atomic scale, Nano Res. 16 (2023) 5626–5639, https://doi.org/10.1007/s12274-022-5135-3.
[24] M.C. Gao, D.B. Miracle, D. Maurice, X. Yan, Y. Zhang, J.A. Hawk, High-entropy functional materials, J. Mater. Res. 33 (2018) 3138–3155, https://doi.org/10.1557/jmr.2018.323.
[25] L. Han, S. Zhu, Z. Rao, et al., Multifunctional high-entropy materials, Nat. Rev. Mater. 9 (2024) 846–865, https://doi.org/10.1038/s41578-024-00720-y.
[26] Y. Yuan, Y. Wu, X. Tong, H. Zhang, H. Wang, X.J. Liu, L. Ma, H.L. Suo, Z.P. Lu, Acta Mater. 125 (2017) 481–489, https://doi.org/10.1016/j.actamat.2016.12.021] Rare-earthhigh-entropyalloyswithgiantmagnetocaloriceffect.
[27] Z. Dong, Z. Wang, S. Yin, Magnetic properties and large cryogenic magneto-caloric effect of Er0.2Tm0.2Ho0.2Cu0.2Co0.2 amorphous ribbon, Intermetallics 124 (2020): 106879, https://doi.org/10.1016/j.intermet.2020.106879.
[28] S.F. Lu, L. Ma, J. Wang, Y.S. Du, L. Li, J.T. Zhao, G.H. Rao, Effect of configuration entropy on magnetocaloric effect of rare earth high-entropy alloy, J. Alloys Compd. 874 (2021): 159918, https://doi.org/10.1016/j.jallcom.2021.159918.
[29] M.S. Lucas, D. Belyea, C. Bauer, N. Bryant, E. Michel, Z. Turgut, S.O. Leontsev, J. Horwath, S.L. Semiatin, M.E. McHenry, C.W. Miller, Thermomagnetic analysis of FeCoCrxNi alloys: magnetic entropy of high-entropy alloys, J. Appl. Phys. 113 (17) (2013) 17A923, https://doi.org/10.1063/1.4798340.
[30] A. Perrin, M. Sorescu, M.T. Burton, D.E. Laughlin, M. McHenry, The role of compositional tuning of the distributed exchange on magnetocaloric properties of high-entropy alloys, JOM 69 (2017) 2125–2129, https://doi.org/10.1007/s11837-017-2523-3.
[31] S.-M. Na, P.K. Lambert, H. Kim, J. Paglione, N.J. Jones, Thermomagnetic properties and magnetocaloric effect of FeCoNiCrAl-type high-entropy alloys, AIP Adv. 9 (3) (2019): 035010, https://doi.org/10.1063/1.5079394.
[32] K. Sarlar, A. Tekgül, I. Kucuk, Magnetocaloric properties in a FeNiGaMnSi high entropy alloy, Curr. Appl. Phys. 20 (2020) 18, https://doi.org/10.1016/j.cap.2019.09.019.
[33] K. Sarlar, A. Tekgül, N. Küçük, A.B. Etemoğlu, Structural and magnetocaloric properties of FeNi high entropy alloys, Phys. Scri. 96 (2021): 125847, https://doi.org/10.1088/1402-4896/ac326d.
[34] J.Y. Law, Á. Díaz-García, L.M. Moreno-Ramírez, V. Franco, Increased magnetocaloric response of FeMnNiGeSi high-entropy alloys, Acta Mater. 212 (2021): 116931, https://doi.org/10.1016/j.actamat.2021.116931.
[35] J.Y. Law, L.M. Moreno-Ramírez, Á. Díaz-García, A. Martín-Cid, S. Kobayashi, S. Kawaguchi, T. Nakamura, V. Franco, MnFeNiGeSi high-entropy alloy with large magnetocaloric effect, J. Alloys Compd. 855 (2021): 157424, https://doi.org/10.1016/j.jallcom.2020.157424.
[36] Y. Guo, T. Zhang, Z. Zhang, B. Chen, W. Guo, S. Pan, Y. Gong, Y. Bai, Y. Gong, J. Liu, X. Miao, F. Xu, Large reversible magnetocaloric effect in high-entropy

MnFeCoNiGeSi system with low-hysteresis magnetostructural transformation, APL Mater. 10 (2022) 9, https://doi.org/10.1063/5.0108367.
[37] Z. Zheng, P. Huang, X. Chen, H. Wang, S. Da, G. Wang, Z. Qiu, D. Zeng, Enhanced magnetocaloric properties of the $(MnNi)_{0.6}Si_{0.62}(FeCo)_{0.4}Ge_{0.38}$ high-entropy alloy obtained by Co substitution, Entropy 26 (2024) 799, https://doi.org/10.3390/e26090799.
[38] Y. Zhang, P. Xu, J. Zhu, S. Yan, J. Zhang, L. Li, The emergence of considerable room temperature magnetocaloric performances in the transition metal high-entropy alloys, Mater. Today Phys. 32 (2023): 101031, https://doi.org/10.1016/j.mtphys.2023.101031.
[39] Alvaro Díaz-García, Jia Yan Law, Luis M. Moreno-Ramírez, Victorino Franco, Stress-relieved Fe-Mn-Ni-Ge-Si high-entropy alloys: a path for enhancing the magnetocaloric response, Scr. Mater. 258 (2025): 116492, https://doi.org/10.1016/j.scriptamat.2024.116492.
[40] Yong Zhang, Ting Ting Zuo, Zhi Tang, Michael C. Gao, Karin A. Dahmen, Peter K. Liaw, Zhao Ping Lu, Microstructures and properties of high-entropy alloys, Prog. Mater. Sci. 61 (2014) 1–93, https://doi.org/10.1016/j.pmatsci.2013.10.001.
[41] G. Porcari, M. Buzzi, F. Cugini, R. Pellicelli, C. Pernechele, L. Caron, E. Brück, M. Solzi, Direct magnetocaloric characterization and simulation of thermomagnetic cycles, Rev. Sci. Instrum. 84 (2013): 073907, https://doi.org/10.1063/1.4815825.
[42] F. Cugini, M. Solzi, Magnetocaloric characterization of materials, Handb. Magn. Mater. 33 (2024) 29–119, https://doi.org/10.1016/bs.hmm.2024.08.001.
[43] T. Stopa, S. Kaprzyk, J. Tobola, Linear aspects of the korringa–kohn–rostoker formalism, J. Phys. Condens. Matter 16 (2004) 4921–4933, https://doi.org/10.1088/0953-8984/16/28/012.
[44] S. Kaprzyk, A. Bansil, Green's function and a generalized Lloyd formula for the density of states in disordered muffin-tin alloys, Phys. Rev. B 42 (1990) 7358–7362, https://doi.org/10.1103/PhysRevB.42.7358.
[45] A. Bansil, S. Kaprzyk, P.E. Mijnarends, J. Toboła, Electronic structure and magnetism of $Fe_{3-x}V_xX$ (X=Si, Ga, and Al) alloys by the KKR-CPA method, Phys. Rev. B 60 (1999) 13396–13412, https://doi.org/10.1103/PhysRevB.60.13396.
[46] W. Steurer, Single-phase high-entropy alloys – a critical update, Mater. Charact. 162 (2020): 110179, https://doi.org/10.1016/j.matchar.2020.110179.
[47] Julian Ledieu, Karine Dumesnil, Mélanie Emo, Sylvie Migot, Sorour Semsari Parapari, Sašo Šturm, Primož Koželj, Vincent Fournée, Epitaxial growth of rare-earth high-entropy alloy thin films, ACS Nano 19 (29) (2025) 26400–26410, https://doi.org/10.1021/acsnano.5c02644.
[48] L. Caron, Z.Q. Ou, T.T. Nguyen, D.T. Cam Thanh, O. Tegus, E. Brück, On the determination of the magnetic entropy change in materials with first-order transitions, J. Magn. Magn Mater. 321 (2009) 3559–3566, https://doi.org/10.1016/j.jmmm.2009.06.086.
[49] G. Porcari, F. Cugini, S. Fabbrici, C. Pernechele, F. Albertini, M. Buzzi, M. Mangia, M. Solzi, Convergence of direct and indirect methods in the magnetocaloric study of first order transformations: the case of Ni-Co-Mn-Ga Heusler alloys, Phys. Rev. B 86 (2012): 104432, https://doi.org/10.1103/PhysRevB.86.104432.
[50] L. Pareti, M. Solzi, F. Albertini, A. Paoluzi, Giant entropy change at the co-occurrence of structural and magnetic transitions in the Ni Mn Ga Heusler alloy, Eur. Phys. J. B 32 (2003) 303, https://doi.org/10.1140/epjb/e2003-00102-y.
[51] W. Guo, X. Miao, J. Cui, S. Torii, F. Qian, Y. Bai, Z. Kou, J. Zha, Y. Shao, Y. Zhang, F. Xu, L. Caron, Significantly enhanced reversibility and mechanical stability in grain-oriented MnNiGe-based smart materials, Acta Mater. 263 (2024): 119530, https://doi.org/10.1016/j.actamat.2023.119530.
[52] P. Entel, V.D. Buchelnikov, V.V. Khovailo, A.T. Zayak, W.A. Adeagbo, M.E. Gruner, H.C. Herper, E.F. Wassermann, Modelling the phase diagram of magnetic shape memory Heusler alloys, J. Phys. D Appl. Phys. 39 (2006) 865–889, https://doi.org/10.1088/0022-3727/39/5/S13.
[53] M.D. Kuz'min, M. Richter, Mechanism of the strong magnetic refrigerant performance of $LaFe_{13-x}Si_x$, Phys. Rev. B 76 (2007): 092401, https://doi.org/10.1103/PhysRevB.76.092401.
[54] H. Yamada, K. Fukamichi, T. Goto, Itinerant-electron metamagnetism and strong pressure dependence of the Curie temperature, Phys. Rev. B 5 (2001): 024413 https://doi.org/0.1103/PhysRevB.65.024413.
[55] A. Fujita, K. Fukamichi, J.-T. Wang, Y. Kawazoe, Large magnetovolume effects and band structure of itinerant-electron metamagnetic $La(Fe_xSi_{1-x})_{13}$ compounds, Phys. Rev. B 68 (2003): 104431, https://doi.org/10.1103/PhysRevB.68.104431.
[56] A. Fujita, H. Yako, Stability of metallic, magnetic and electronic states in $NaZn_{13}$-type $La(Fe_xSi_{1-x})_{13}$ magnetocaloric compounds, Scr. Mater. 67 (2012) 578, https://doi.org/10.1016/j.scriptamat.2012.03.033.
[57] K. Rudolph, A.K. Pathak, Y. Mudryk, V.K. Pecharsky, Magnetostructural phase transitions and magnetocaloric effect in $(Gd_{5-x}Sc_x)Si_{1.8}Ge_{2.2}$, Acta Mater. 145 (2018) 369–376, https://doi.org/10.1016/j.actamat.2017.12.024.
[58] S.A. Nikitin, A.V. Smirnov, I.A. Ovchenkov, The influence of titanium substitution on the magnetic, magnetocaloric, and magnetoelastic properties of $Gd_5Si_2Ge_2$, J. Appl. Phys. 124 (2018): 083902, https://doi.org/10.1063/1.5036723.